

Highly Stretchable and Reconfigurable Ionogels with Unprecedented Thermoplasticity and Ultrafast Self-Healability Enabled by Gradient-Responsive Networks

Yufeng Wang, Ying Liu, Roshan Plamthottam, Mike Tebyetekerwa, Jingsan Xu, Jixin Zhu, Chao Zhang,* and Tianxi Liu*

Cite This: *Macromolecules* 2021, 54, 3832–3844

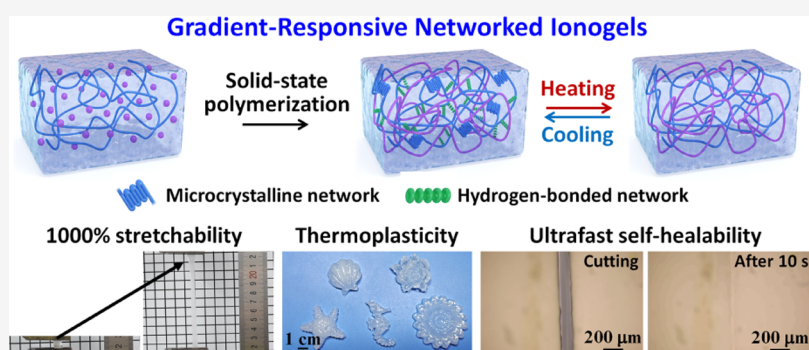
Read Online

ACCESS |

Metrics & More

Article Recommendations

Supporting Information



ABSTRACT: Nonvolatile and durable ionogels are emerging and promising stretchable ionic conductors for wearable electronics. However, the construction of reconfigurable and recyclable ionogels with high mechanical robustness, high stretchability, and autonomous healability, while heavily demanded, is very challenging. Here, we present a gradient-responsive cross-linking strategy for preparing a highly stretchable and reconfigurable thermoplastic engineering ionogel (TPEI). The design of both microcrystalline and dense hydrogen bonds in TPEI contributed to the formation of a unique gradient-responsive network. When the TPEI was melt-processed under heating, the microcrystalline network structure was destroyed to form entangled polymer chains, while the high-density hydrogen-bonded network structure was only partially destroyed. The remaining hydrogen-bonded network allowed the TPEI to have a high viscosity for melt processing. When the TPEI was cooled upon melting injection, extrusion, and spinning, the hydrogen-bonded network was rapidly reconstructed in tens of seconds, allowing it to be reconfigured and reshaped, while the microcrystalline network was further reconstructed to improve its mechanical strength and elasticity during subsequent aging. As a result, the TPEI exhibited engineering-hydrogel-level mechanical robustness (>100 kPa), extremely high stretchability (>1000%), wide-temperature tolerance (−20 to 80 °C), and ultrafast self-healability in few seconds. Due to its mechanical adaptability, high ionic conductivity, and reconfigurability, the TPEI was demonstrated to readily work as a self-healable and recyclable stretchable conductor in a wearable skin-inspired sensor for monitoring sophisticated human motions.

1. INTRODUCTION

Artificial skins are an emerging field of bionics, aiming to intelligently imitate tactile sensing characteristics of human skin.^{1–3} Ionic conductors such as ionogels and hydrogels that are stretchable, mechanically adaptable, and optically transparent have been used to realize functions of ionic skin (i-skin) with human skin perception characteristics.^{4–11} They can effectively sense external stimuli including pressure, strain, and torsion.^{12–14} However, i-skins need to withstand large and complex deformations in practical applications, putting forward high requirements for ionic conductors with mechanically robust and adaptable characteristics.^{15–18} i-skins also may potentially undergo continuous mechanical loading in a variety of temperatures and humidities. This can result in mechanical degradation and largely reduced service life,^{19–21} which

inevitably leads to electronic waste and environmental pollution.^{22–24} Furthermore, i-skins can hardly maintain their initial high sensitivity in a wide range of stress/temperatures, and thus, it is hard for them to gain universal acceptance.²⁵ Therefore, the achievement of ionic conductors with high mechanical strength, self-healability, and extreme-temperature tolerance is critical to the development of i-skin for next-

Received: February 24, 2021

Revised: March 30, 2021

Published: April 14, 2021



generation human–computer interaction, soft robotics, and health monitoring.

An ionogel is a three-dimensional polymer network hosted in ionic liquids (ILs).^{26–28} Ionogels are popular owing to their softness and high ion-conductive properties.^{29–31} Ionogels not only inherit the advantages of ILs including high thermal stability,³² chemical inertness,³³ and excellent ionic conductivity^{34,35} but also have additional advantages of mechanical flexibility and high stretchability.^{36,37} Therefore, functionality-designed ionogels have wide prospects in sensors,^{28,38} solid electrolytes,^{39–41} actuators,⁴² and many other applications.^{24,43,44} However, conventional ILs are expensive and toxic, which greatly limits their use in wearable i-skins.⁴⁵ Furthermore, the enhancements in mechanical strength of ionogels can be achieved through the design of stable chemical bonding and covalent cross-linking structures and the loss of subsequent secondary processability which undoubtedly leads to resource waste and plastic pollution at the end of their use.⁴⁶ Therefore, the development of reconfigurable and recyclable ionogels with high mechanical strength and low toxicity is of great need for the new generation of i-skin.

Herein, a gradient-responsive cross-linking strategy is presented for preparing a thermoplastic engineering ionogel (TPEI) with ultrastretchability and high ionic conductivity that can self-heal rapidly. The hypothesis revolved around the design of a physically dual-cross-linked ionogel network with gradient-responsive rates, resulting in its highly reconfigurable and recyclable features *via* repeated melting–curing cycles. The gradient-responsive cross-linking among the TPEI contributed to its high mechanical strength, ultrastretchability, and ultrafast self-healability under ambient conditions. The microcrystalline network structure among the TPEI was destroyed to form entangled polymer chains during melt processing, while the dense hydrogen-bonded network allowed the TPEI to have a high viscosity for melt processing. When the TPEI was cooled upon melting injection, extrusion, and spinning, the hydrogen-bonded network was rapidly reconstructed in tens of seconds, allowing it to be reconfigured and reshaped, while the microcrystalline network was further reconstructed to improve its mechanical strength and elasticity during subsequent aging. The gradient-responsive cross-linking allowed the TPEI to exhibit a mechanically robust yet autonomous self-healable performance at room temperature, together with a fast melt-solid phase transition at a high temperature that enabled its recyclable and reconfigurable features. As a proof-of-concept, a TPEI-based skin-inspired sensor was fabricated and demonstrated high sensitivity in monitoring physiological signals of human healthcare and activities in a wide temperature range with ultrafast autonomous self-healability.

2. RESULTS AND DISCUSSION

A representative TPEI sample that consisted of a dynamic hydrogen-bonded network and polyvinyl alcohol (PVA) microcrystalline network was fabricated through a gradient-responsive cross-linking strategy. A semi-crystalline PVA, acrylamide (AAM) monomer, and its photoinitiator were dissolved in a choline chloride/ethylene glycol deep eutectic solvent (ChCl–EG DES) at 130 °C, and gelation with a fast melt-solid phase transition was produced when cooled down to room temperature. The ChCl–EG DES showed higher ionic conductivity than those of traditional ILs (1-butyl-3-methyl-

imidazolium tetrafluoroborate, 1-butyl-3-methylimidazolium bis((trifluoromethyl)sulfonyl)imide, *etc.*)⁴⁷ Besides, the ChCl–EG DES with abundant hydrogen donors and acceptors facilitated the easy dissolution of PVA chains (Figure S1, Supporting Information), and such high-concentration dissolution of PVA was unimaginable in traditional ILs. Then, polyacrylamide (PAAm) chains were *in situ*-formed among the solid-state DES-swollen PVA network under a UV-initiated photopolymerization at room temperature. The TPEI-1, TPEI-2, and TPEI-3 represent the mass ratio of PVA to PAAm within the TPEI of 3:4, 3:8, and 3:12, respectively. Upon aging, the gradient-responsive networks among the TPEI were achieved (Figure 1a). The as-formed linear PAAm would

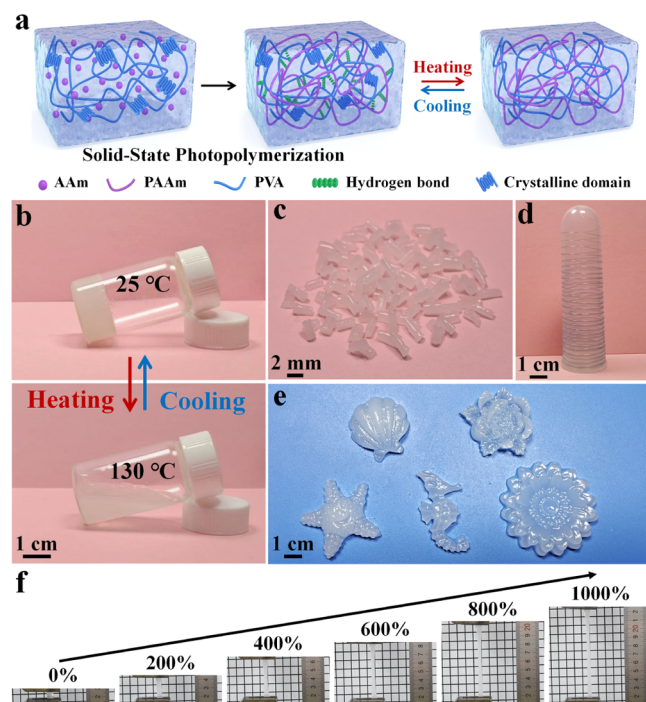


Figure 1. Design principle and fabrication of the melt-processable and reconfigurable TPEI. (a) Schematic illustration of the TPEI by gradient-responsive cross-linking. (b) Slant vial method showing the thermal reversibility of TPEI. (c) TPEI pellets prepared by melt extrusion and pelletizing. (d) TPEI fiber coils prepared by melt spinning. (e) TPEI in diverse shapes prepared by melt injection. (f) TPEI samples stretched at a strain from 0 to 1000%.

interact with both the PAAm chains and PVA chains through intermolecular hydrogen-bonded interactions. ¹H nuclear magnetic resonance (NMR) spectroscopy of AAM monomers and TPEI was performed. The ¹H NMR spectrum of AAM monomers showed peaks at 5.7–6.5 ppm ascribed to hydrogen atoms among the acrylate double bonds (Figure S2a, Supporting Information). However, the peaks at 5.7–6.5 ppm disappeared in the ¹H NMR spectrum of TPEI, and the appeared peaks at 1.1–2.3 ppm were ascribed to hydrogen atoms of the PAAm (Figure S2b, Supporting Information).⁴⁸ The results indicated that the initial AAM monomers were completely polymerized within the solid-state network of DES-swollen PVA. The energy-dispersive X-ray spectrometry (EDS) mappings showed homogeneously distributed C, N, and O elements among the solvent-free TPEI (Figure S3, Supporting Information). Additionally, a stable and dense network of PVA *via* its microcrystalline domains was formed in sequence. As a

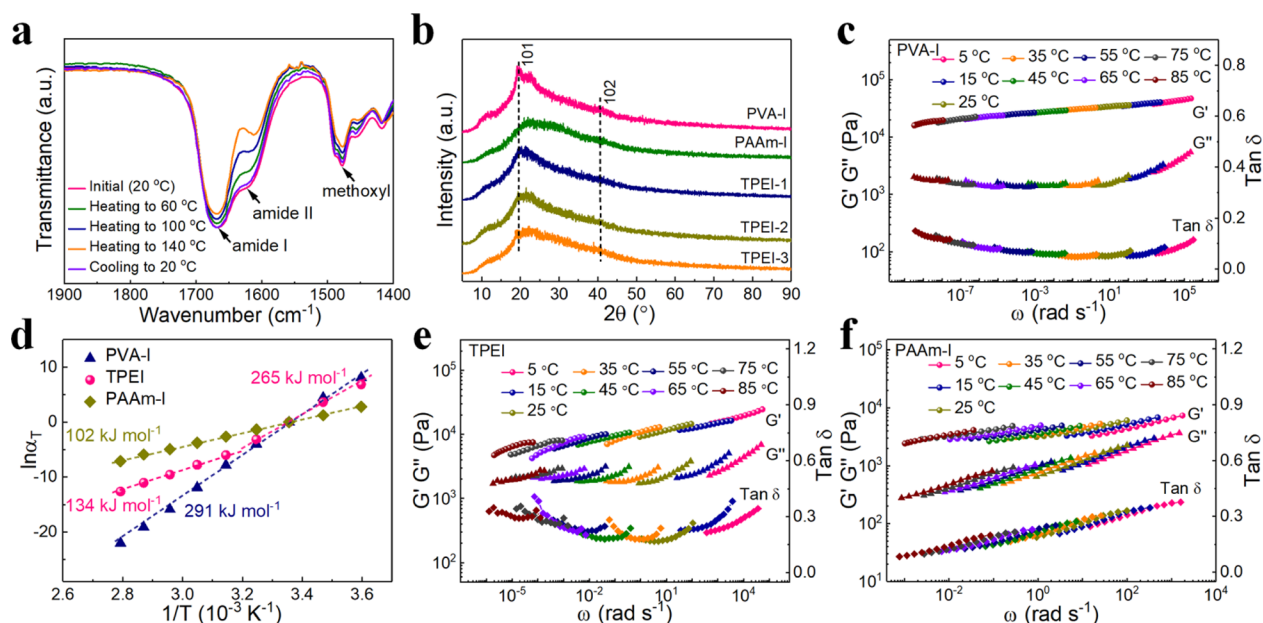


Figure 2. Characterization of gradient-responsive network structures among the TPEI. (a) Variable-temperature FT-IR spectra of TPEI-2. (b) X-ray diffraction (XRD) patterns of TPEI, PVA-I, and PAAm-I. Frequency dependence of the storage modulus G' , loss modulus G'' , and loss factor $\tan \delta$ of (c) PVA-I. (d) Activation energy derived from Arrhenius plots for shift factors of TPEI-2, PVA-I, and PAAm-I. Frequency dependence of the storage modulus G' , loss modulus G'' , and loss factor $\tan \delta$ of (e) TPEI-2 and (f) PAAm-I.

result, the temperature linear-dependent hydrogen bonding and temperature step-dependent microcrystalline domains in the TPEI resulted in high stretchability and excellent mechanical strength at room temperature and showed thermoplasticity at high temperature.

Figure 1b shows the temperature-dependent invertible sol-gel transition of the TPEI, verified by the slant vial method. The TPEI kept the gel state with a fixed shape at room temperature, while it changed from the gel to sol state when the temperature increased to 130 °C. The TPEI exhibited a fast and highly reversible melt-solid phase transition process. The TPEI in the sol state would retransform into its solid-state without extra stimuli (*i.e.*, liquid-nitrogen freezing and quenching) when it recooled to room temperature. The intriguing thermoplasticity of the TPEI facilitated a unique recycling and reconfigurable behavior (Movie S1, Supporting Information). The pellets of TPEI were easily obtained by melt extrusion and pelletizing using a conventional extruder granulator (Figure 1c), and the TPEI pellets are capable of being remelted at 130 °C and then extruded into fiber samples through a melt-spinning extruder (Figure 1d). The TPEI also showed excellent reconfigurability by melt-injecting into a variety of shapes, that is, shell, seahorse, starfish, sunflower, and rose (Figure 1e). Besides, Figure 1f showed that the TPEI can be stretched to 1000%, indicating its excellent stretchability (Movie S2, Supporting Information).

The formation of the gradient-responsive networks among the TPEI is vital to its unique thermoplasticity and largely enhanced mechanical robustness. Figure S4a (Supporting Information) shows the formation of hydrogen-bonded interactions between the PVA and PAAm chains within the TPEI that caused the peak shift in the Fourier transform infrared (FT-IR) spectrum.^{49–51} The FT-IR spectrum of the PVA ionogel (PVA-I) had peaks at 3331 and 1092 cm^{-1} , which were assigned to the $-\text{OH}$ stretching region and $\text{C}-\text{O}-\text{C}$ symmetric stretching, respectively. For the PAAm ionogel

(PAAm-I), four distinct peaks appeared at 3353, 3179, 1658, and 1615 cm^{-1} , which were ascribed to $-\text{NH}_2$ asymmetric stretching, $-\text{NH}_2$ symmetric stretching, and symmetric stretching of amide I and amide II, respectively.^{52,53} The TPEI also showed the absorption peaks of PVA-I and PAAm-I in the FT-IR spectra. Compared to the PVA-I and PAAm-I, the absorption peaks corresponding to $-\text{OH}$ and $-\text{NH}_2$ stretching in the region of 3100–3400 cm^{-1} were overlapped and shifted, exhibiting peaks at 3345 cm^{-1} , which indicated the formation of hydrogen bonds between the PVA and PAAm in the TPEI. The absorption peaks corresponding to amide I and amide II bands of solvent-free TPEI were red-shifted compared with those of TPEI, indicating the hydrogen bond formation between the ChCl-EG DES and polymer backbones (Figure S4b, Supporting Information). Strong hydrogen-bonded interactions between the ChCl-EG and polymer backbones efficiently avoided the leakage of liquid ChCl-EG DES. The absorption peaks of hydrogen donors of the $-\text{OH}$ and $-\text{NH}_2$ stretching of solvent-free TPEI in the range of 3100–3400 cm^{-1} were also shifted compared with those of solvent-free PVA and PAAm samples, further indicating the formation of hydrogen bonds between the PVA and PAAm chains within the TPEI.

To characterize the temperature-sensitive dynamic hydrogen bonding of TPEI, temperature-dependent FT-IR was performed (Figure 2a). As the hydrogen donors of $-\text{OH}$ and $-\text{NH}_2$ stretching of TPEI in the region of 3100–3400 cm^{-1} were overlapped, the shifting of the absorption peaks in the region of 1400–1800 cm^{-1} was critically studied. As the temperature increased from 20 to 140 °C, the intensity of infrared absorption peaks of the amide I and amide II bands decreased (Table 1). The absorption peak corresponding to amide I showed a blue shift from 1665 to 1668 cm^{-1} when the temperature increased from 20 to 140 °C. The results showed that the hydrogen bonds of TPEI were dissociated and weakened with the increasing temperature.⁵⁴ The temperature-

Table 1. Normalized Intensity of the FT-IR Peak (Amide I and Amide II) and XRD Pattern Varied with an Increasing Temperature

temperature (°C)	normalized intensity of the FT-IR peak	temperature (°C)	normalized intensity of the diffraction pattern at 20 deg
20	1	20	1
60	0.94	50	0.99
100	0.86	80	0.89
140	0.76	110	0.58

dependent dissociation process of hydrogen bonds was approximately linearly related to the temperature. Besides, when the temperature decreased from 140 to 20 °C at a cooling rate of 10 °C min⁻¹, the intensity and center of absorption peaks of amide I and amide II returned to the initial state, indicating that the hydrogen bonds were rapidly and completely regenerated.

The XRD patterns of PVA-I and TPEI samples showed a peak located at 2θ of $\sim 20^\circ$, corresponding to the (101) plane of PVA, and a broad peak at 2θ of $20\text{--}30^\circ$ was observed to be assigned to the amorphous PAAm and PVA (Figure 2b).³⁹ The temperature-dependent XRD patterns of the TPEI-2 showed that the intensity of the characteristic pattern did not decrease significantly when the temperature increased from 20 to 80 °C, suggesting the good stability of the crystalline domains of PVA at the low temperature (Figure S5 in the Supporting Information and Table 1). When temperature continued to increase to 110 °C, the intensity of the characteristic peak decreased, indicating that the crystalline domains were dissociated. The results showed that the crystalline domains of the dissociation process were step-dependent with temperature. The intensity of the characteristic peak was partially restored when the temperature dropped to 20 °C at a rate of 10 °C min⁻¹, indicating the regeneration of the crystalline domains among the TPEI.

The differential scanning calorimetry (DSC) curves of PVA-I and TPEI samples showed a melting peak at a temperature of $\sim 115^\circ\text{C}$ when the temperature increased from 20 to 140 °C (Figure S6a, Supporting Information), corresponding to the melting of microcrystalline domains of the TPEI.⁵⁵ Figure S6b (Supporting Information) shows the DSC cooling thermograms of TPEI. A crystallization peak at $\sim 55^\circ\text{C}$ was observed in the DSC curves, corresponding to the recrystallization of TPEI. Compared with the PVA-I, the dried PVA powder showed stronger melting-crystallization peaks and higher melting temperature than that of PVA-I in the DSC curves, indicating that the ChCl-EG decreased the crystalline domains and increased the segmental mobility of PVA (Figure S7, Supporting Information). The crystallinity of PVA-I and TPEI samples tested by XRD and DSC are summarized in Table 2. With the increase in PAAm content in TPEI, the crystallinity of TPEI decreased, indicating that PAAm

Table 2. Crystallinity (χ_c) and Melting Enthalpy (ΔH_m) of TPEI and PVA-I Calculated from DSC and XRD Results

sample	χ_c (%) from DSC	ΔH_m (J g ⁻¹)	χ_c (%) from XRD
PVA-I	4.3	5.9	6.4
TPEI-1	2.6	3.6	4.3
TPEI-2	1.5	2.1	3.1
TPEI-3	0.3	0.42	1.9

effectively regulated the rigidity and enhanced the mechanical toughness of TPEI. Figure S8 (Supporting Information) shows the peaks of melting and crystallization for TPEI-2 in four continuous units of heating-cooling operation. The intensity of the melting peak in the fourth cycle decreased only slightly compared with that in the first cycle, indicating excellent reversible thermoplasticity of the TPEI-2. Squeezing tests were measured to compare the compatibility between the ChCl-EG DES and polymer backbones (Figure S9, Supporting Information). When the TPEI sample was squeezed, there was no leaked liquid ChCl-EG DES on the weighing paper. However, when the PVA-I sample was squeezed, the liquid ChCl-EG DES leaked on the weighing paper, indicating that the ChCl-EG DES had good and poor compatibilities with polymer backbones among the TPEI and PVA-I, respectively (Figure S9, Supporting Information). The excellent compatibility between the ChCl-EG DES and polymer backbones within the TPEI is attributed to enhanced hydrogen-bonded interactions between PVA and ChCl-EG DES due to its reduced crystallinity restricted by PAAm chains. Owing to the gradient-responsive networks of microcrystalline domains and hydrogen bonds, the TPEI exhibited unique thermoplasticity and reconfigurability.

The mechanical strength and rheological performance of the TPEI with dynamic hydrogen bonds were also investigated. The PVA-I, PAAm-I, and TPEI followed the time-temperature superposition. The dynamic behaviors of the ionogels at different frequencies and temperatures of the reference temperature at 25 °C (constructed by nine frequency sweeps performed at 5, 15, 25, 35, 45, 55, 65, 75, and 85 °C) were investigated. The storage modulus (G') of PVA-I exhibited a weak frequency dependence and a low loss factor ($\tan \delta$) in a wide frequency range (Figure 2c). The $\tan \delta$ of PVA-I gradually increased when the frequency decreased and reached a balanced range at 3×10^{-8} rad s⁻¹ with a relaxation time of $\sim 5 \times 10^6$ s. The apparent activation energy (E_a) for the flow of PVA-I was estimated by the Arrhenius equation (E_a of 291 kJ mol⁻¹) with the frequency-scale shift factor (α_T) (Figure 2d). The ultralong relaxation time and high E_a of PVA-I indicate that PVA-I processes have abundant strong interactions, which were derived from the microcrystalline domains in PVA. Compared with PVA-I, the G' of TPEI showed obvious frequency dependence (Figure 2e). The $\tan \delta$ of TPEI showed two peaks at frequencies of 8.5×10^{-6} (relaxation time: $\sim 2 \times 10^4$ s) and 200 rad s⁻¹ (relaxation time: 8×10^{-4} s). These two E_a of 134 and 256 kJ mol⁻¹ of TPEI were obtained from the Arrhenius plots, indicating that TPEI existed with two bonds with different strengths. The two different bonding strengths originated from the PVA and PAAm interpenetrating network structure among the TPEI, in which the microcrystalline domains of PVA and the hydrogen bonds between PVA and PAAm acted as the strong and weak bonds, respectively. The $\tan \delta$ of PAAm-I gradually increased with the increase in the frequency (Figure 2f) and reached a peak at 800 rad s⁻¹ (a relaxation time of $\sim 8 \times 10^{-4}$ s). The short relaxation time of PAAm-I indicated that the hydrogen bonds within the PAAm-I were weak, and the E_a of 102 kJ mol⁻¹ of PAAm was observed from the Arrhenius plot.

The TPEI with gradient-responsive networks showed a renewable and reconfigurable performance. To illustrate the thermoplasticity of TPEI, a temperature-dependent rheology test was carried out. Figure 3a shows that the G' and G'' of PVA-I had a weak temperature dependence when the

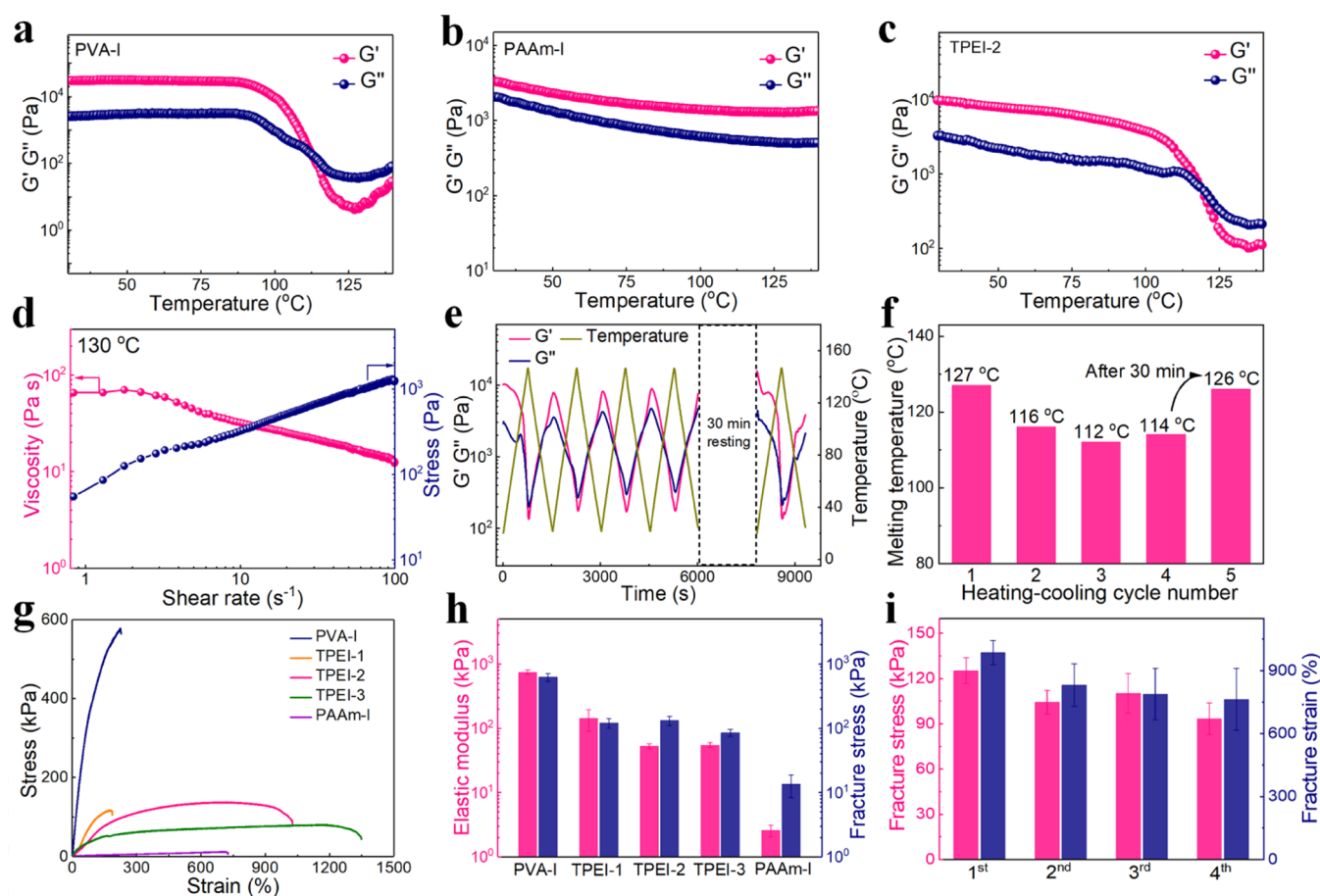


Figure 3. Mechanical performance of the TPEI. Temperature dependence of G' and G'' for (a) PVA-I, (b) PAAm-I, and (c) TPEI-2. (d) Shear-thinning behavior of TPEI-2 at 130 °C. (e) G' and G'' values of TPEI-2 in a reversible temperature-dependent rheological test. (f) Melting temperatures of TPEI-2 from the reversible temperature-dependent rheological test in five melting/curing cycles. (g) Typical tensile stress–strain curves of PVA-I, TPEI, and PAAm-I. (h) Elastic modulus and fracture stress of PVA-I, TPEI, and PAAm-I. (i) Fracture stress and fracture strain of TPEI-2 in melting and curing cycles.

temperature was lower than 80 °C. When the temperature increased to 140 °C, the G' of PVA rapidly dropped to the 10^0 level, and a sol–gel transition occurred at a temperature of 112 °C, indicating that the physically cross-linked network was damaged. In contrast, the G' and G'' of PAAm-I gradually decreased with the increase in temperature, and no sol–gel transition occurred (Figure 3b). This difference came from the microcrystalline domains in the PVA network, which made PVA-I show a solid-like behavior at ambient temperature and a sol state when the microcrystalline domains broke at high temperatures. The TPEI with different PVA–PAAm ratios displayed different rheological performances (Figures 3c and S10, Supporting Information). The G' of TPEI-2 showed a slight decline when the temperature was below 100 °C, which was attributed to the dissociation of hydrogen bonds, and exhibited a sol–gel transition at a temperature of 123 °C, attributing to the melting of microcrystalline domains. The result showed that the TPEI-2 had a stable mechanical performance at room temperature, and the physically cross-linked networks could be uncoupled at high temperatures, introducing a convenient strategy for reuse and recycling. Noteworthy, the G' of TPEI-2 was higher than that of PVA-I at a temperature of 130 °C, attributing to the denser hydrogen bonding network in TPEI than PVA. This provided the necessary viscosity for the melt injection of TPEI. With increasing content of PAAm in the TPEI, the sol–gel transition

temperature gradually increased until the TPEI-3 lost the sol–gel transition behavior. Furthermore, the shear-thinning behavior of the TPEI at 130 °C was suitable for melt injection (Figure 3d), indicating the potential of TPEI for melt state processing techniques. The temperature-dependent rheological test of TPEI-2 was measured (Figure 3e), revealing the reversibility of the G' and G'' values and repeatable gel–sol–gel transition, which indicated the repeatable thermoplastic performance of TPEI-2. The temperature-dependent rheological test also showed that the temperature for the sol–gel transition of TPEI-2 in the first cycle appeared at 127 °C, while the temperature appeared at 116, 112, and 114 °C, respectively, during the continuous up–down second–fourth temperature cycles (Figure 3f). During the cooling stage, the sol–gel transition temperature of TPEI-2 was lower than the temperature during the heating stage. This was explained that the physically cross-linked network in the TPEI could not be completely restored in time. Moreover, the sol–gel transition temperatures appeared at 126 °C when the fifth cycle was applied 30 min later. Internal damage was almost completely healed by resting the TPEI-2 at 20 °C for a period of time before reheating. The result indicated that the TPEI had excellent thermoplasticity with repeatable thermo-reversible mechanical properties.

The as-fabricated TPEI is very stretchable with excellent mechanical strength due to a strong–weak physically cross-

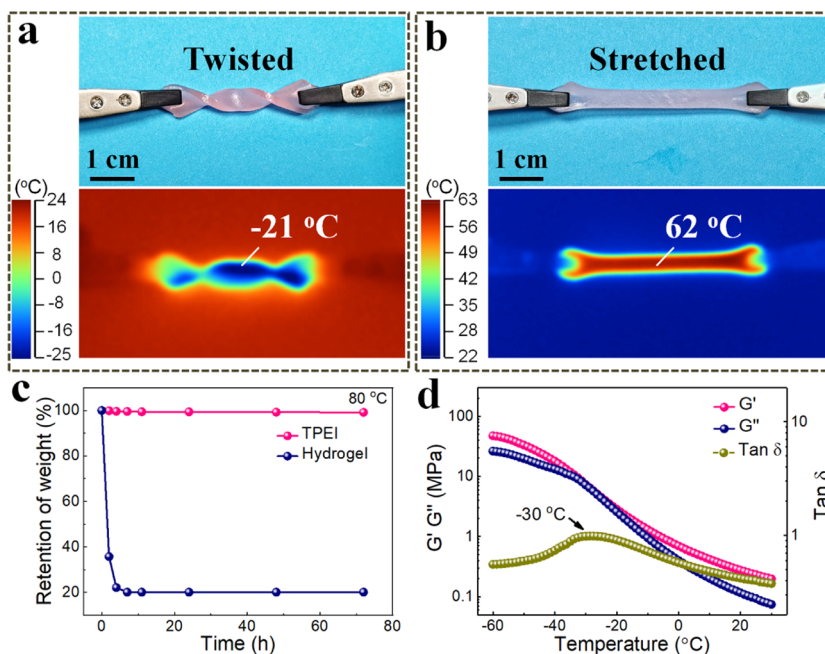


Figure 4. Extreme-temperature tolerance of the TPEI. Photographs and infrared images of TPEI-2 that is (a) twisted at $-25\text{ }^{\circ}\text{C}$ and (b) stretched at $70\text{ }^{\circ}\text{C}$. Before photographing, all the samples were aged for 12 h at the temperature. (c) Weight retention of TPEI-2 and hydrogel samples as a function of time at $80\text{ }^{\circ}\text{C}$. (d) Dependence of G' , G'' , and $\tan\delta$ vs temperature for TPEI-2.

linked network of hydrogen bonding and microcrystalline domains. The tensile stress–strain curves of PVA-I, PAAm-I, and TPEIs are shown in Figure 3g. The PVA-I exhibited a high elastic modulus ($\sim 0.72\text{ MPa}$) and fracture strength ($\sim 0.58\text{ MPa}$) but poor elongation at break ($\sim 200\%$), while the PAAm-I showed a low fracture strength ($\sim 12\text{ kPa}$) and high elongation at break ($\sim 730\%$). High elastic modulus and poor elongation of PVA-I were attributed to the microcrystalline network structure, which limited the movement of the polymer chain network. The elastic modulus gradually decreased when the PAAm content within the TPEI increased. Compared with TPEI-2 and TPEI-3, the TPEI-1 showed a low elongation at break, contributing to the fact that the content of PAAm in the TPEI-1 was too low to form a continuous network (Figure 3h). To confirm this, scanning electron microscopy (SEM) images of PVA-I, PAAm-I, and TPEIs are shown in Figure S11 (Supporting Information). The PVA-I showed a sheet-backboned polymer skeleton (Figure S11a–c, Supporting Information), and the PAAm-I presented an ordered grid structure (Figure S11m–o, Supporting Information). The TPEI showed a sheet-backboned PVA structure linked with the grid structure of PAAm (Figure S11d–l, Supporting Information). When the content of PAAm was low in TPEI, the PVA was locally stacked and not connected with PAAm, which led to the poor mechanical properties in TPEI-1. With the increased PAAm content in TPEI, the two network components were fully bound and interpenetrated within each other. As a result, the TPEI-2 showed an excellent mechanical performance with $\sim 135\text{ kPa}$ tensile strength and $\sim 1030\%$ elongation at break (6.1 wt % PVA and 16.2 wt % PAAm in TPEI-2). The excellent mechanical performance of TPEI-2 was attributed to the effective energy dissipation of abundant hydrogen bonds, as well as the rigid microcrystalline region of PVA as a sacrificial fracture. Tensile stress–strain curves of TPEI with various solid contents were measured. Compared with the TPEI-2 with a 24% solid content (TPEI-24%), the

TPEI-2 with a 30% solid content (TPEI-30%) exhibited a high tensile strength of $\sim 164\text{ kPa}$ but with a low elongation at break of $\sim 480\%$, while the TPEI-2 with a 16% solid content (TPEI-16%) showed a low tensile strength and elongation at break of $\sim 74\text{ kPa}$ and 610% (Figure S12, Supporting Information), respectively. The largely reduced elongation at break of TPEI-30% was ascribed to limited movements of polymer segments due to the high-content polymer backbones among the TPEI-2. The poor mechanical performance of TPEI-16% was attributed to the insufficient cross-linking density of the physically cross-linked network due to the low content of polymer backbones among the TPEI-2. In successive tensile fatigue tests at a 100% strain, the TPEI-2 showed a decreased fracture stress and a small plastic deformation ($<10\%$) during 500 cycles, indicating an excellent fatigue resistance of TPEI-2 (Figure S13, Supporting Information). The recyclability assessment of TPEI-2 was determined by measuring the recovery of fracture stress and fracture strain after melting–curing cycles (Figure 3i). It was notable that for the TPEI-2, even after four cycles of melting and curing, the values of fracture stress and fracture strain remained $\sim 80\%$, which demonstrated the excellent reversible thermoplasticity of the TPEI. Tensile stress–strain curves of the TPEI-2 samples aged for various days [$25\text{ }^{\circ}\text{C}$, relative humidity (RH) value of 80%] were measured. The TPEI-2 samples upon aging for various days (0–10 days) showed similar tensile stress–strain curves (Figure S14, Supporting Information), indicating the long-term mechanical stability of the as-prepared TPEI-2 samples.

An extremely temperature-tolerant performance of the TPEI under both high and low temperatures is achieved, demonstrating its high reconfigurable performance and excellent stability during the secondary melt-processing processes. The TPEI-2 showed high flexibility that endured twisting after storing it at $-25\text{ }^{\circ}\text{C}$ for 12 h (Figure 4a) and stretching at 300% after storing at $70\text{ }^{\circ}\text{C}$ for 12 h (Figure 4b). In contrast, the PVA–PAAm hydrogel lost its flexibility at

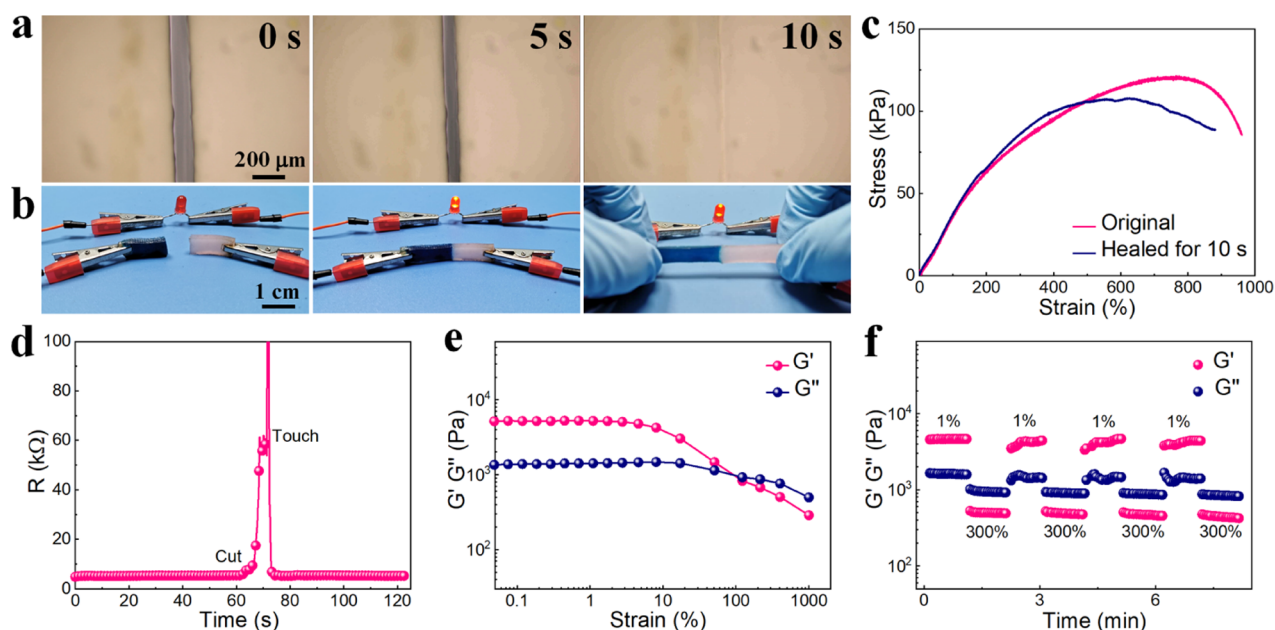


Figure 5. Self-healing property of the TPEI. (a) Time-dependent optical micrographs of TPEI-2 upon cutting. (b) Photographs showing two fractured TPEI samples to lighten up an LED in a circuit after self-healing and stretching. (c) Comparison of tensile stress–strain curves of TPEI-2 before and after self-healing. (d) Recovery of ionic conductivity of TPEI-2 upon cutting and self-healing. (e) Strain sweep measurements of TPEI-2 from 0.05 to 1000%. (f) Continuous step-strain sweep for TPEI-2 with an alternating oscillatory of 1 and 300%.

temperatures of -25 and 70 °C and failed during twisting and stretching. To further illustrate the extreme temperature tolerance, the mass loss of the TPEI-2 at 80 °C was tested for 72 h (Figure 4c). Only a very little amount of mass loss was observed in the TPEI-2 ($<1\%$) caused by the high-density hydrogen-bonded interaction of ChCl–EG with polymer chains, which effectively prevented the decomposition and evaporation of species. However, the PVA–PAAm hydrogel lost almost all its moisture after being placed at 80 °C for only 10 h.

The dynamic mechanical analysis (DMA) measurement of the PVA–PAAm hydrogel and TPEI-2 was conducted at a temperature of -60 to 30 °C (Figures 4d, S15, Supporting Information). For the PVA–PAAm hydrogel, the G' and G'' decreased rapidly when the temperature increased to 4 °C, which was attributed to the melting of ice crystals and the TPEI-2 changing from the glassy state to the elastic state. In contrast, the TPEI-2 had a transition temperature of -30 °C, indicating that the TPEI-2 had a lower freezing point than that of the PVA–PAAm hydrogel. The extreme tolerance in a wide temperature range of TPEI-2 with high elasticity effectively prevented changing from rigid and fragile when the TPEI-2 was used in the cold and dry environment. Furthermore, the ionic conductivity of TPEI-2 showed long-term stability (~ 0.3 S m^{-1}) for 7 days at 25 °C (Figure S16, Supporting Information). The ionic conductivity of the TPEI-2 was 0.12 – 2.47 S m^{-1} in the temperature range from -10 to 90 °C, indicating that the TPEI-2 showed high stability in a wide temperature range (Figure S17, Supporting Information). Figure S18 (Supporting Information) shows that the TPEI sample had a high and stable ionic conductivity even though it was melted and cured for five cycles.

Unlike permanent and stable covalent bonding, the TPEI with dynamic hydrogen bonds is highly reversible, allowing the self-healing of TPEI upon damages. The self-healing process of TPEI-2 was observed by time-dependent optical micrographs

in Figure 5a and Movie S3 (Supporting Information) at a constant temperature of 25 °C by simulating the room temperature. The crack between two fractured TPEI-2 samples gradually decreased in a very short period and mostly disappeared in 10 s, indicating an extremely fast self-healing performance of TPEI-2. Figure 5b shows a circuit connected with a piece of the TPEI-2 sample, and a light-emitting diode (LED) can be lighted by a 5 V driving voltage. The LED was extinguished, when the TPEI-2 was cut into two parts. When the two parts of TPEI-2 came into contact with each other with a tiny force and recombined a complete circuit, the LED was illuminated again. The brightness of the LED darkened when the healed TPEI-2 was stretched. The results indicated the rapid healing of mechanical and electrical properties of the TPEI-2.

To further study the self-healing ability of TPEI-2, the tensile stress–strain performance of healed TPEI-2 was tested (Figure 5c, Movie S4, Supporting Information). When the two pieces of TPEI-2 were combined and self-healed into a whole body, the fracture strain and tensile strength of the repaired TPEI-2 were restored to 91.7 and 90.5% of those before cutting, respectively. The tensile stress–strain curves of the TPEI-2 showed that an elastic modulus and elongation at break only decreased slightly when it was cut and healed three times, further indicating that the TPEI-2 had an excellent self-healing ability (Figure S19, Supporting Information). The capability of the electrical recovery of TPEI-2 is shown in Figure 5d, 99% of the electrical recovery in 10 s. The strain amplitude sweep test of TPEI-2 is shown in Figure 5e,f to evaluate the self-healing ability. At a low oscillatory strain, the storage moduli (G') were much higher than loss moduli (G''), and the TPEI-2 behaved like an elastic solid (Figure 5e). In contrast, G'' was higher than G' at a high oscillatory strain, indicating that the physically cross-linked network was damaged at a high strain. To confirm this, the *in situ* FT-IR spectra are shown in Figure S20 (Supporting Information). As

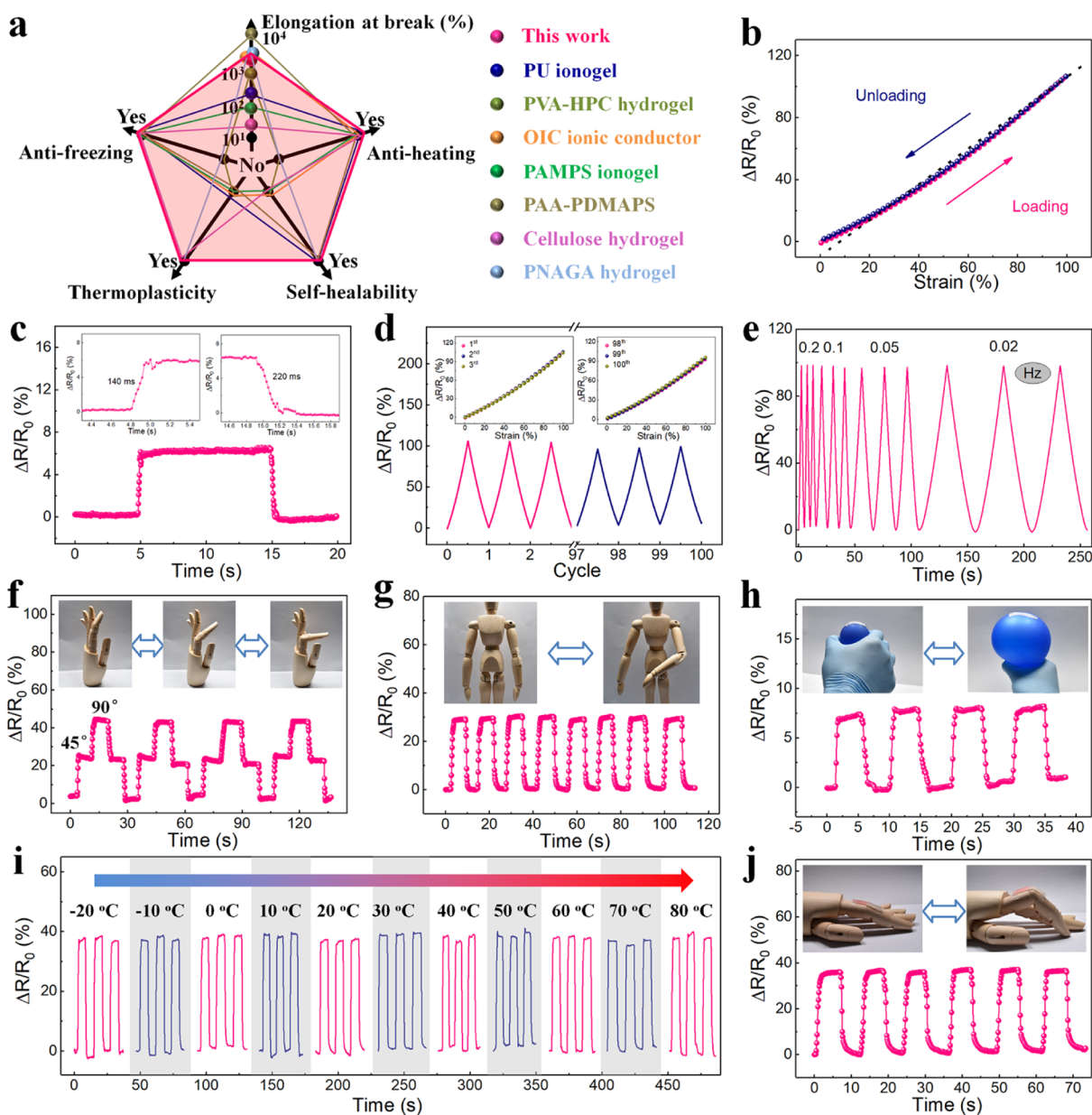


Figure 6. Wearable TPEI resistance sensor detecting complex mechanical motions. (a) Comparison between TPEI and previously reported ionic conductors in terms of thermoplasticity, self-healability, antifreezing/antiheating ability, and elongation ratio. (b) Relative resistance variations during loading/unloading cycles. (c) Relative resistance variations with an instantaneous strain. Insets in (c) show the response and recovery time. (d) Relative resistance variations upon stretching to 100% strain for 100 cycles. Insets in (d) show the relative resistance variations for 1st–3rd and 98th–100th cycles. (e) Relative resistance variations at various loading frequencies upon stretching to 100% strain. Relative resistance variations of the sensor device fixed on (f) prosthetic finger-monitoring bending angles, (g) prosthetic elbow-monitoring bending angles, and (h) a balloon-monitoring heaving movement. (i) Relative resistance variations of prosthetic finger bending at various temperatures. (j) Relative resistance variations of prosthetic finger bending after cutting and self-healing.

the oscillatory strain increased from 1 to 1000%, the intensity of absorption peaks of amide I and amide II decreased, indicating that the hydrogen-bonded network was destroyed. In contrast, the oscillatory strain decreased from 1000 to 1% and the corresponding peak intensity returned to the initial state, indicating the rapid healing of the hydrogen-bonded network among the TPEI. Continuous step-strain sweeps with alternate low-amplitude oscillatory (1%) and high-amplitude oscillatory (300%) of the TPEI-2 are shown in Figure 5f. At the first sequence, the G' was higher than G'' under the low-amplitude oscillatory, and the G' experienced a dramatic drop that was lower than the G'' when at a high-amplitude

oscillatory (300%). When the oscillatory strain returned to 1%, the G' and G'' of TPEI-2 were recovered mostly in a very short time, and the behavior could be cycled multiple times, which further illustrates the rapid self-healing ability of TPEI-2.

The intriguing properties with mechanically adaptable irregular interfaces, excellent temperature tolerance, and self-healing ability of TPEI are ideal for use in skin-inspired sensors as an ionic conductor (Figure 6a).^{4,7,26,56–59} Figure 6b depicts the TPEI resistance sensor exhibiting a reversibly linear relationship between resistance and strain between 0 to 100% strain, and the gauge factor (GF) value of the TPEI resistance sensor was ~ 1.07 . The TPEI resistance sensor also

showed a high response to a large strain of 300% (Figure S21, Supporting Information). The response time of the TPEI resistance sensor was investigated upon 10% tensile strain applied instantaneously (Figure 6c), showing a short response time (~ 140 ms) and recovery time (~ 220 ms). The durability test of the TPEI resistance sensor revealed the stability of the resistance change and reversible linear relationship between resistance and strain in 100 cycles, indicating excellent reliability of the TPEI resistance sensor (Figure 6d). Figure 6e shows that a continuous and stable resistance response upon 100% tensile strain with a frequency ranging from 0.02 to 0.2 Hz was achieved, indicating that the TPEI resistance sensor was not influenced by the frequency of the applied stress. As a proof-of-concept, a wearable TPEI resistance sensor was applied to detect human motion and biomedical signals such as finger motion, knee motion, and respiratory activity. Figure 6f exhibits that the TPEI resistance sensor was used to precisely monitor the prosthetic finger straightening–bending process with different bending angles (45 and 90°). The shape of $\Delta R/R_0$ time curves remained almost unchanged for four cycles under the bending angles, indicating good durability of the TPEI resistance sensor. Besides, the intensity of the signal response was related to the bending angles. The amplitudes increased with the increasing bending angle, indicating that the TPEI resistance sensor could differentiate the angles of joint motion. Figures 6g, S22, and 23 (Supporting Information) show that the TPEI resistance sensor attached to the joints was also capable of detecting the bending motions of a puppet, that is, elbow joint, wrist joint, and knee joint of human body. Figure 6h shows that the TPEI resistance sensor was attached to the top of the balloon, and the heaving caused by the swelling and contraction of a balloon was monitored in real time. Moreover, the TPEI resistance sensor showed an excellent sensing performance in the temperature range of -20 to 80 °C (Figures 6i, S24, Supporting Information). The TPEI resistance sensor was fixed on a prosthetic finger to monitor stable joint motion (bending angles 90°) at different temperatures. The device showed an initial resistance decrease with the increase in temperature and kept a relatively stable $\Delta R/R_0$ value at different temperatures, which indicates that the TPEI resistance sensor can be used under extreme temperature conditions.⁶⁰ Besides, the reliability of the TPEI resistance sensor under damaged conditions was evaluated. When two fractured TPEI were in contact with each other and assembled in a resistance sensor, the healed device responded well to bending–straightening motions of the prosthetic finger (Figure 6j). Overall, the TPEI can play a vital role in new-generation flexible sensors, with the advantages of reversible thermoplasticity, self-healing ability, and excellent temperature tolerance.

3. CONCLUSIONS

This work described a mechanically robust yet highly stretchable ionogel (TPEI) via a gradient-responsive cross-linking strategy. The TPEI used the ChCl–EG as an ionic plasticizer, which not only effectively plasticized the TPEI but also greatly improved its temperature tolerance, enabling TPEI to be used at extreme temperatures or reshape and recycle at high temperatures. Benefiting from the temperature-responsive dynamic microcrystalline domain and hydrogen bonds, the TPEI exhibited a reversible sol–gel transition under the stimulation of temperature, achieving reprocessing and recyclable properties of TPEI and reducing the waste of resources. Besides, the as-prepared TPEI showed high

stretchability (1030%) and excellent mechanical strength (135 kPa) at room temperature, which was ascribed to the effective energy dissipation of the stiff microcrystalline domains and ductile hydrogen-bonded network. With processability, ionic conductivity, self-healability, and high stretchability, the TPEI is an interesting candidate for a novel generation of flexible sensing materials. As a proof-of-concept, the TPEI resistance sensor can monitor human motions (e.g., finger bending, facial muscle motions, and breathing). Our studies might open a new avenue to fabricate a thermoplastic ionogel for thermoplastic, healable, and recyclable i-skin.

4. EXPERIMENTAL PROCEDURES

4.1. Materials. AAm (99%), ChCl (99%), 1-butyl-3-methylimidazolium tetrafluoroborate ([BMIM]BF₄, 99%), and 1-butyl-3-methylimidazolium bis((trifluoromethylsulfonyl)imide) ([BMIM]-TF₂N, 99%) were obtained from Adamas. PVA ($M_w = 85,000$ – $124,000$, 99+% hydrolyzed) and EG (anhydrous, 99.8%) were purchased from Sigma-Aldrich. 2,2-Diethoxyacetophenone (DEAP) (95%) was provided by TCI. Deionized (DI) water was used in all experiments.

4.2. Preparation of TPEI. The ChCl–EG DES was prepared by mixing the ChCl and EG with a 1:2 molar ratio at 70 °C under stirring for 10 min. The PVA powder (0.30 g) was dissolved into 3.5 mL of ChCl–EG DES at 130 °C under stirring in a nitrogen atmosphere until being completely dissolved, and then, a designed amount of AAm (5.7–17.1 mmol) and DEAP (2 wt % of AAm) was added under stirring at 130 °C. The mixed solution was transferred into a poly(tetrafluoroethylene) (PTFE) mold ($50 \times 5 \times 2$ mm³), cooled to 25 °C, cured under a UV light (CL-1000L, $\lambda = 365$ nm, power: 8 W) for 1 h, and left in a humidity chamber (40 °C, RH: 60%) for 12 h to complete the photopolymerization reaction. For comparison, the PVA–PAAm hydrogel was prepared using water instead of ChCl–EG as the solvent. Neat PAAm-I was prepared by dissolving AAm (17.1 mmol) in 3.5 mL of ChCl–EG DES, and other conditions are the same as the TPEI. The PVA-I was prepared by dissolving 0.30 g of PVA powder in 3.5 mL of ChCl–EG DES at 130 °C under stirring until being completely dissolved, and the solution was transferred into a PTFE mold to solidify and shape at room temperature. The TPEI pellets were obtained by melting, extruding, and pelletizing using an extruder (RZC-3331), and the TPEI pellets can be remelted at 130 °C and then extruded into a long fiber through an extruder. The shapes of TPEI (shell, seahorse, starfish, sunflowers, and roses) were tailored by melting in an extruder at 130 °C and melt-injecting into various molds.

4.3. Material Characterization. Pore structures and EDS mappings of TPEI samples were measured by field-emission scanning electron microscopy (FESEM, JSM-7500F). Before FESEM tests, solvent-free TPEI samples were fabricated by soaking in excess DI water for solvent exchange and subsequently freeze-drying. ¹H NMR spectra of TPEI and AAm were recorded on an AVANCE III 600 MHz NMR spectrometer using D₂O as the solvent. FT-IR spectra were measured on a Magna-IR750 FT-IR spectrometer in the range of 4000 – 400 cm⁻¹. Temperature-dependent FT-IR spectra were measured from 20 to 140 °C at a heating rate of 5 °C min⁻¹. *In situ* FT-IR spectra of alternating step-strain sweeps of TPEI samples were tested by alternating 1 and 1000% shear strains. XRD patterns of TPEI samples were measured using an X-ray diffractometer with a Ni-filtered Cu K α (40 kV, 35 mA, DY-1291). Temperature-dependent XRD patterns were measured from 20 to 110 °C at a heating/cooling rate of 10 °C min⁻¹. Rheological behaviors of TPEI samples were measured using a HAAKE MARS rheometer using a 25 mm parallel-plate geometry and investigated at an angular frequency (ω) ranging from 1 to 100 rad s⁻¹ at a fixed oscillatory strain of 1%. Temperature-dependent rheological behaviors were measured from 20 to 140 °C at a heating–cooling rate of 10 °C min⁻¹ at an angular frequency and fixed oscillatory strain of 10 rad s⁻¹ and 1%, respectively. Dynamic mechanical behaviors of TPEI samples at different temperatures (5,

15, 25, 35, 45, 55, 65, 75, and 85 °C, reference temperature at 25 °C) were measured at an angular frequency ranging from 1 to 100 rad s⁻¹ at a fixed oscillatory strain of 1%. The apparent activation energy (E_a) for the flow of TPEI samples were estimated by the Arrhenius equation, $\alpha_T = A e^{E_a/RT}$, where α_T is the shift factor, A is a constant, and R is the ideal gas constant. The alternate step-strain sweeps of TPEI samples were performed by alternating 1 and 300% shear strains four times at a fixed frequency of 10 rad s⁻¹. Tensile tests of TPEI samples (10 × 5 × 2 mm³) were performed on a universal testing machine (SANS, Shenzhen, China) and recorded at a tensile rate of 20 mm min⁻¹. All the tensile measurements were tested at room temperature, and the samples were placed in a humidity chamber (30 °C, RH: 80%) for 12 h before the tests. For qualitatively demonstrating the self-healing performance, the TPEI sample was cut into two pieces and made to come into contact with each other with a tiny force for 10 s. Optical microscopy images and movies of fractured and healed TPEI samples were evaluated using an optical microscope at 25 °C (BX-51, Olympus). DMA measurement (Q800, TA) was carried out in a temperature range of -60 to 30 °C at a heating rate of 5 °C min⁻¹, and the strain and frequency were set at 0.1% and 1 Hz, respectively. The weight retentions of TPEI and hydrogel samples under high temperatures were tested by putting TPEI and PVA-PAAm hydrogel samples into a humidity chamber at 80 °C.

The crystallinity (χ_c) of TPEI samples was calculated from DSC and XRD results.

The χ_c from DSC results was calculated using eq 1

$$\chi_c = \frac{\Delta H_m}{\Delta H_0} \quad (1)$$

where ΔH_m is the melting enthalpy of TPEI samples and ΔH_0 is the enthalpy of PVA crystals (138.6 J g⁻¹).

The χ_c from XRD results was calculated using eq 2

$$\chi_c = \frac{\sum A_{\text{cryst}}}{\sum A_{\text{cryst}} + \sum A_{\text{amor}}} \quad (2)$$

where A_{amor} and A_{cryst} are the areas of amorphous and crystals phases among the XRD patterns, respectively.

4.4. Measurements of the TPEI Resistance Sensor. The resistive-type strain sensing device was assembled with two copper foil current collectors sandwiched with a TPEI sample (30 × 10 × 2 mm³), and the copper foil current collectors were used for connecting the testing wires. The TPEI resistive strain sensor was sealed in VHB tape (3M 4905). The resistance from the strain sensor was measured on a Keithley 2616 System source meter at a voltage of 3 V. The temperature-dependent resistive-type strain sensing performances of TPEI samples were tested in a humidity chamber with tailored temperatures from -20 to 80 °C. The TPEI sensors were adhered to the finger, knee, wrist, and elbow of a puppet and the balloon to instantaneously detect diagnosis for simulation of complex human motions. The $\Delta R/R_0$ was calculated using eq 3

$$\frac{\Delta R}{R_0} = \frac{R - R_0}{R_0} \quad (3)$$

where R and R_0 are the real-time and initial resistances, respectively.

The GF value was calculated using eq 4

$$\text{GF} = \frac{\Delta R/R_0}{\varepsilon} \quad (4)$$

where ε is the applied strain.

■ ASSOCIATED CONTENT

Supporting Information

The Supporting Information is available free of charge at <https://pubs.acs.org/doi/10.1021/acs.macromol.1c00443>.

Photographs showing the PVA powder dissolved in various ILs at 130 °C; ¹H NMR spectra of AAm and TPEI; SEM image and the corresponding C, O, and N EDS mappings of TPEI-2 after solvent exchange with excess water and freeze-drying; FT-IR spectra of TPEI, PAAm-I, PVA-I, solvent-free TPEI, solvent-free PAAm-I, and solvent-free PVA-I; temperature-dependent XRD patterns of the TPEI; DSC heating and cooling thermograms of PAAm-I, PVA-I, and TPEI; DSC curves of neat PVA; DSC curves of TPEI-2 in four continuous heating-cooling cycles; photographs showing TPEI and PVA-I squeezed on a weighting paper; temperature-dependent rheological measurements of TPEI-1 and TPEI-3; FESEM images of PVA-I, TPEI-1, TPEI-2, TPEI-3, and PAAm-I after the solvent exchange with excess water and freeze-drying; tensile stress-strain curves of TPEI with various solid contents; tensile fatigue tests of TPEI-2 at a 100% strain for 500 cycles; tensile stress-strain curves of TPEI-2 aged at room temperature for various time; temperature dependence of G' , G'' , and $\tan \delta$ for the PVA-PAAm hydrogel; ionic conductivity of TPEI-2 aged for 7 days at room temperature; ionic conductivity of TPEI-2 after multiple melting-curing cycles; tensile stress-strain curves of TPEI-2 after multiple cutting and healing cycles; ionic conductivity of TPEI-2 as a function of temperature; *in situ* FT-IR spectra of alternate step-strain sweep for the TPEI-2; relative resistance changes in TPEI-2 during tensile loading/unloading at strains between 100 and 300%; relative resistance changes in the TPEI-2 sensor that was fixed on a prosthetic wrist joint for detecting its bending; relative resistance changes in the TPEI-2 sensor that was fixed on a prosthetic knee joint for detecting its bending; and resistance changes in the TPEI-2 sensor detecting finger bending at different ambient temperatures (PDF)

Thermoplasticity of TPEI with reconfigurable behavior (AVI)

TPEI stretched to 1000% (AVI)

Crack between fractured TPEI gradually self-healing (AVI)

Tensile performance of fractured TPEI after extremely fast self-healing (AVI)

■ AUTHOR INFORMATION

Corresponding Authors

Chao Zhang – State Key Laboratory for Modification of Chemical Fibers and Polymer Materials, College of Materials Science and Engineering, Innovation Center for Textile Science and Technology, Donghua University, Shanghai 201620, P. R. China; orcid.org/0000-0003-1255-7183; Email: czhang@dhu.edu.cn

Tianxi Liu – State Key Laboratory for Modification of Chemical Fibers and Polymer Materials, College of Materials Science and Engineering, Innovation Center for Textile Science and Technology, Donghua University, Shanghai 201620, P. R. China; Key Laboratory of Synthetic and Biological Colloids, Ministry of Education, School of Chemical and Material Engineering, Jiangnan University, Wuxi 214122, P. R. China; orcid.org/0000-0002-5592-7386; Email: txliu@fudan.edu.cn

Authors

Yufeng Wang – State Key Laboratory for Modification of Chemical Fibers and Polymer Materials, College of Materials Science and Engineering, Innovation Center for Textile Science and Technology, Donghua University, Shanghai 201620, P. R. China

Ying Liu – State Key Laboratory for Modification of Chemical Fibers and Polymer Materials, College of Materials Science and Engineering, Innovation Center for Textile Science and Technology, Donghua University, Shanghai 201620, P. R. China

Roshan Plamthottam – Soft Materials Research Laboratory, Department of Materials Science and Engineering, Henry Samueli School of Engineering and Applied Science, University of California, Los Angeles, Los Angeles, California 90095, United States

Mike Tebyetekerwa – Research School of Electrical, Energy and Materials Engineering, The Australian National University, Canberra, Australian Capital Territory 2601, Australia; orcid.org/0000-0002-4243-6043

Jingsan Xu – School of Chemistry, Physics and Mechanical Engineering, Queensland University of Technology, Brisbane, Queensland 4001, Australia; orcid.org/0000-0003-1172-3864

Jixin Zhu – Shaanxi Institute of Flexible Electronics (SIFE), Northwestern Polytechnical University (NPU), Xi'an 710072, P. R. China; orcid.org/0000-0001-8749-8937

Complete contact information is available at:

<https://pubs.acs.org/10.1021/acs.macromol.1c00443>

Author Contributions

C.Z. and T.L. conceived the work and cowrote the manuscript. Y.W., C.Z., and T.L. designed and performed the experiments and analyzed the data. Y.L. assisted with the strain sensing measurements. M.T., R.P., J.X., and J.Z. analyzed the data and wrote the manuscript. All authors have given approval to the final version of the manuscript.

Notes

The authors declare no competing financial interest.

ACKNOWLEDGMENTS

The authors acknowledge funding support from the National Natural Science Foundation of China (21875033), the Shanghai Rising-Star Program (18QA1400200), Ministry of Education of the People's Republic of China (6141A02033233), and the Shanghai Scientific and Technological Innovation Project (18JC1410600).

REFERENCES

- (1) Zhang, H.; Cong, Y.; Osi, A. R.; Zhou, Y.; Huang, F.; Zaccaria, R. P.; Chen, J.; Wang, R.; Fu, J. Direct 3D Printed Biomimetic Scaffolds Based on Hydrogel Microparticles for Cell Spheroid Growth. *Adv. Funct. Mater.* **2020**, *30*, 1910573.
- (2) Du, G.; Mao, A.; Yu, J.; Hou, J.; Zhao, N.; Han, J.; Zhao, Q.; Gao, W.; Xie, T.; Bai, H. Nacre-Mimetic Composite with Intrinsic Self-Healing and Shape-Programming Capability. *Nat. Commun.* **2019**, *10*, 800.
- (3) Zhao, X.; Chen, F.; Li, Y.; Lu, H.; Zhang, N.; Ma, M. Bioinspired Ultra-Stretchable and Anti-Freezing Conductive Hydrogel Fibers with Ordered and Reversible Polymer Chain Alignment. *Nat. Commun.* **2018**, *9*, 3579.
- (4) Zhou, Y.; Wan, C.; Yang, Y.; Yang, H.; Wang, S.; Dai, Z.; Ji, K.; Jiang, H.; Chen, X.; Long, Y. Highly Stretchable, Elastic, and Ionic

Conductive Hydrogel for Artificial Soft Electronics. *Adv. Funct. Mater.* **2019**, *29*, 1806220.

(5) Ma, R.; Chou, S.-Y.; Xie, Y.; Pei, Q. Morphological/Nanostructural Control toward Intrinsically Stretchable Organic Electronics. *Chem. Soc. Rev.* **2019**, *48*, 1741–1786.

(6) Guo, Y.; Bae, J.; Fang, Z.; Li, P.; Zhao, F.; Yu, G. Hydrogels and Hydrogel-Derived Materials for Energy and Water Sustainability. *Chem. Rev.* **2020**, *120*, 7642–7707.

(7) Lei, Z.; Wu, P. A. Highly Transparent and Ultra-Stretchable Conductor with Stable Conductivity During Large Deformation. *Nat. Commun.* **2019**, *10*, 3429.

(8) Li, R. A.; Chen, G.; Fan, T.; Zhang, K.; He, M. Transparent Conductive Elastomers with Excellent Autonomous Self-Healing Capability in Harsh Organic Solvent Environments. *J. Mater. Chem. A* **2020**, *8*, 5056–5061.

(9) Ren, Y.; Guo, J.; Liu, Z.; Sun, Z.; Wu, Y.; Liu, L.; Yan, F. Ionic Liquid-Based Click-Ionogels. *Sci. Adv.* **2019**, *5*, No. eaax0648.

(10) Matsuda, T.; Nakajima, T.; Gong, J. P. Fabrication of Tough and Stretchable Hybrid Double-Network Elastomers Using Ionic Dissociation of Polyelectrolyte in Nonaqueous Media. *Chem. Mater.* **2019**, *31*, 3766–3776.

(11) An, M.; Zhang, Q.; Lin, Y.; Wang, D.; Chen, W.; Meng, L.; Yin, P.; Li, L. Stretch-Induced Reverse Brill Transition in Polyamide 46. *Macromolecules* **2020**, *53*, 11153–11165.

(12) Gan, D.; Huang, Z.; Wang, X.; Jiang, L.; Wang, C.; Zhu, M.; Ren, F.; Fang, L.; Wang, K.; Xie, C.; Lu, X. Graphene Oxide-Templated Conductive and Redox-Active Nanosheets Incorporated Hydrogels for Adhesive Bioelectronics. *Adv. Funct. Mater.* **2019**, *30*, 1907678.

(13) Cao, Z.; Liu, H.; Jiang, L. Transparent, Mechanically Robust, and Ultrastable Ionogels Enabled by Hydrogen Bonding between Elastomers and Ionic Liquids. *Mater. Horiz.* **2020**, *7*, 912–918.

(14) Niu, S.; Matsuhisa, N.; Beker, L.; Li, J.; Wang, S.; Wang, J.; Jiang, Y.; Yan, X.; Yun, Y.; Burnett, W.; Poon, A. S. Y.; Tok, J. B.-H.; Chen, X.; Bao, Z. A Wireless Body Area Sensor Network Based on Stretchable Passive Tags. *Nat. Electron.* **2019**, *2*, 361–368.

(15) Zhang, H. J.; Sun, T. L.; Zhang, A. K.; Ikura, Y.; Nakajima, T.; Nonoyama, T.; Kurokawa, T.; Ito, O.; Ishitobi, H.; Gong, J. P. Tough Physical Double-Network Hydrogels Based on Amphiphilic Triblock Copolymers. *Adv. Mater.* **2016**, *28*, 4884–4890.

(16) Pan, L.; Wang, F.; Cheng, Y.; Leow, W. R.; Zhang, Y. W.; Wang, M.; Cai, P.; Ji, B.; Li, D.; Chen, X. A Supertough Electro-Tendon Based on Spider Silk Composites. *Nat. Commun.* **2020**, *11*, 1332.

(17) Zhang, Q.; Zhang, R.; Meng, L.; Ji, Y.; Su, F.; Lin, Y.; Li, X.; Chen, X.; Lv, F.; Li, L. Stretch-Induced Structural Evolution of Poly (Vinyl Alcohol) Film in Water at Different Temperatures: An in-Situ Synchrotron Radiation Small- and Wide-Angle X-Ray Scattering Study. *Polymer* **2018**, *142*, 233–243.

(18) Tang, X.; Tian, F.; Xu, T.; Li, L.; Reinhardt, A. Numerical Calculation of Free-Energy Barriers for Entangled Polymer Nucleation. *J. Chem. Phys.* **2020**, *152*, 224904.

(19) Du, W.; Zhang, J.; Zhao, Z.; Zhang, X. Preparation of Novel Temperature-Responsive Double-Network Hydrogel Reinforced with Aramid Nanofibers. *Compos. Commun.* **2020**, *22*, 100438.

(20) Ru, Y.; Fang, R.; Gu, Z.; Jiang, L.; Liu, M. Reversibly Thermosecreting Organogels with Switchable Lubrication and Anti-Icing Performance. *Angew. Chem., Int. Ed.* **2020**, *59*, 11876–11880.

(21) Li, H.; Lv, T.; Sun, H.; Qian, G.; Li, N.; Yao, Y.; Chen, T. Ultrastretchable and Superior Healable Supercapacitors Based on a Double Cross-Linked Hydrogel Electrolyte. *Nat. Commun.* **2019**, *10*, 536.

(22) Qu, G.; Li, Y.; Yu, Y.; Huang, Y.; Zhang, W.; Zhang, H.; Liu, Z.; Kong, T. Spontaneously Regenerative Tough Hydrogels. *Angew. Chem., Int. Ed.* **2019**, *58*, 10951–10955.

(23) Chen, Y.; Tang, Z.; Liu, Y.; Wu, S.; Guo, B. Mechanically Robust, Self-Healable, and Reprocessable Elastomers Enabled by Dynamic Dual Cross-Links. *Macromolecules* **2019**, *52*, 3805–3812.

- (24) Yu, H.; Feng, Y.; Gao, L.; Chen, C.; Zhang, Z.; Feng, W. Self-Healing High Strength and Thermal Conductivity of 3D Graphene/Pdms Composites by the Optimization of Multiple Molecular Interactions. *Macromolecules* **2020**, *53*, 7161–7170.
- (25) Lai, F.; Yang, C.; Lian, R.; Chu, K.; Qin, J.; Zong, W.; Rao, D.; Hofkens, J.; Lu, X.; Liu, T. Three-Phase Boundary in Cross-Coupled Micro-Mesoporous Networks Enabling 3D-Printed and Ionogel-Based Quasi-Solid-State Micro-Supercapacitors. *Adv. Mater.* **2020**, *32*, 2002474.
- (26) Li, T.; Wang, Y.; Li, S.; Liu, X.; Sun, J. Mechanically Robust, Elastic, and Healable Ionogels for Highly Sensitive Ultra-Durable Ionic Skins. *Adv. Mater.* **2020**, *32*, 2002706.
- (27) Ming, X.; Shi, L.; Zhu, H.; Zhang, Q. Stretchable, Phase-Transformable Ionogels with Reversible Ionic Conductor-Insulator Transition. *Adv. Funct. Mater.* **2020**, *30*, 2005079.
- (28) Bai, N.; Wang, L.; Wang, Q.; Deng, J.; Wang, Y.; Lu, P.; Huang, J.; Li, G.; Zhang, Y.; Yang, J.; Xie, K.; Zhao, X.; Guo, C. F. Graded Intrafillable Architecture-Based Iontronic Pressure Sensor with Ultra-Broad-Range High Sensitivity. *Nat. Commun.* **2020**, *11*, 209.
- (29) Wu, S.; Cai, C.; Li, F.; Tan, Z.; Dong, S. Deep Eutectic Supramolecular Polymers: Bulk Supramolecular Materials. *Angew. Chem., Int. Ed.* **2020**, *59*, 11871–11875.
- (30) Li, R. A.; Fan, T.; Chen, G.; Zhang, K.; Su, B.; Tian, J.; He, M. Autonomous Self-Healing, Antifreezing, and Transparent Conductive Elastomers. *Chem. Mater.* **2020**, *32*, 874–881.
- (31) Lee, J.; Tan, M. W. M.; Parida, K.; Thangavel, G.; Park, S. A.; Park, T.; Lee, P. S. Water-Processable, Stretchable, Self-Healable, Thermally Stable, and Transparent Ionic Conductors for Actuators and Sensors. *Adv. Mater.* **2020**, *32*, 1906679.
- (32) Ruiz-Olles, J.; Slavik, P.; Whitelaw, N. K.; Smith, D. K. Self-Assembled Gels Formed in Deep Eutectic Solvents: Supramolecular Eutectogels with High Ionic Conductivity. *Angew. Chem., Int. Ed.* **2019**, *58*, 4173–4178.
- (33) Shi, L.; Jia, K.; Gao, Y.; Yang, H.; Ma, Y.; Lu, S.; Gao, G.; Bu, H.; Lu, T.; Ding, S. Highly Stretchable and Transparent Ionic Conductor with Novel Hydrophobicity and Extreme-Temperature Tolerance. *Research* **2020**, *2020*, 2505619.
- (34) Li, R. a.; Fan, T.; Chen, G.; Xie, H.; Su, B.; He, M. Highly Transparent, Self-Healing Conductive Elastomers Enabled by Synergistic Hydrogen Bonding Interactions. *Chem. Eng. J.* **2020**, *393*, 124685.
- (35) Shang, Y.; Wu, C.; Hang, C.; Lu, H.; Wang, Q. Hofmeister-Effect-Guided Ionohydrogel Design as Printable Bioelectronic Devices. *Adv. Mater.* **2020**, *32*, 2000189.
- (36) Lai, J. C.; Li, L.; Wang, D. P.; Zhang, M. H.; Mo, S. R.; Wang, X.; Zeng, K. Y.; Li, C. H.; Jiang, Q.; You, X. Z.; Zuo, J. L. A Rigid and Healable Polymer Cross-Linked by Weak but Abundant Zn(II)-Carboxylate Interactions. *Nat. Commun.* **2018**, *9*, 2725.
- (37) Wang, Y.; Yu, Y.; Guo, J.; Zhang, Z.; Zhang, X.; Zhao, Y. Bio-Inspired Stretchable, Adhesive, and Conductive Structural Color Film for Visually Flexible Electronics. *Adv. Funct. Mater.* **2020**, *30*, 2000151.
- (38) Xie, C.; Wang, X.; He, H.; Ding, Y.; Lu, X. Mussel-Inspired Hydrogels for Self-Adhesive Bioelectronics. *Adv. Funct. Mater.* **2020**, *30*, 1909954.
- (39) Li, L.; Zhang, Y.; Lu, H.; Wang, Y.; Xu, J.; Zhu, J.; Zhang, C.; Liu, T. Cryopolymerization Enables Anisotropic Polyaniline Hybrid Hydrogels with Superelasticity and Highly Deformation-Tolerant Electrochemical Energy Storage. *Nat. Commun.* **2020**, *11*, 62.
- (40) Huang, S.; Wan, F.; Bi, S.; Zhu, J.; Niu, Z.; Chen, J. A Self-Healing Integrated All-in-One Zinc-Ion Battery. *Angew. Chem., Int. Ed.* **2019**, *58*, 4313–4317.
- (41) Yu, L.; Zhang, Y.; Wang, J.; Gan, H.; Li, S.; Xie, X.; Xue, Z. Lithium Salt-Induced in Situ Living Radical Polymerizations Enable Polymer Electrolytes for Lithium-Ion Batteries. *Macromolecules* **2021**, *54*, 874–887.
- (42) Liu, K.; Zhang, Y.; Cao, H.; Liu, H.; Geng, Y.; Yuan, W.; Zhou, J.; Wu, Z. L.; Shan, G.; Bao, Y.; Zhao, Q.; Xie, T.; Pan, P. Programmable Reversible Shape Transformation of Hydrogels Based on Transient Structural Anisotropy. *Adv. Mater.* **2020**, *32*, 2001693.
- (43) Wang, C.; Zhang, P.; Xiao, W.; Zhao, J.; Shi, M.; Wei, H.; Deng, Z.; Guo, B.; Zheng, Z.; Yu, Y. Visible-Light-Assisted Multimechanism Design for One-Step Engineering Tough Hydrogels in Seconds. *Nat. Commun.* **2020**, *11*, 4694.
- (44) Chen, F.; Zhou, D.; Wang, J.; Li, T.; Zhou, X.; Gan, T.; Handschuh-Wang, S.; Zhou, X. Rational Fabrication of Anti-Freezing, Non-Drying Tough Organohydrogels by One-Pot Solvent Displacement. *Angew. Chem., Int. Ed.* **2018**, *57*, 6568–6571.
- (45) Yang, C.; Suo, Z. Hydrogel Iontronics. *Nat. Rev. Mater.* **2018**, *3*, 125–142.
- (46) Lei, Z.; Huang, J.; Wu, P. Traditional Dough in the Era of Internet of Things: Edible, Renewable, and Reconfigurable Skin-Like Iontronics. *Adv. Funct. Mater.* **2020**, *30*, 1908018.
- (47) Zhang, S.; Sun, N.; He, X.; Lu, X.; Zhang, X. Physical Properties of Ionic Liquids: Database and Evaluation. *J. Phys. Chem. Ref. Data* **2006**, *35*, 1475–1517.
- (48) Mukherjee, M.; Chatterjee, S. K.; Brar, A. S.; Dutta, K. Compositional and Stereochemical Analysis of Acrylamide/Vinyl Acetate Copolymers by One- and Two-Dimensional NMR Spectroscopy. *Macromolecules* **1998**, *31*, 8455–8462.
- (49) Wang, A.; Wang, Y.; Zhang, B.; Wan, K.; Zhu, J.; Xu, J.; Zhang, C.; Liu, T. Hydrogen-Bonded Network Enables Semi-Interpenetrating Ionic Conductive Hydrogels with High Stretchability and Excellent Fatigue Resistance for Capacitive/Resistive Bimodal Sensors. *Chem. Eng. J.* **2021**, *411*, 128506.
- (50) Wang, Y.; Tebyetekerwa, M.; Liu, Y.; Wang, M.; Zhu, J.; Xu, J.; Zhang, C.; Liu, T. Extremely Stretchable and Healable Ionic Conductive Hydrogels Fabricated by Surface Competitive Coordination for Human-Motion Detection. *Chem. Eng. J.* **2020**, 127637.
- (51) Zhang, B.; Zhang, X.; Wan, K.; Zhu, J.; Xu, J.; Zhang, C.; Liu, T. Dense Hydrogen-Bonding Network Boosts Ionic Conductive Hydrogels with Extremely High Toughness, Rapid Self-Recovery and Autonomous Adhesion for Human-Motion Detection. *Research* **2021**, 2021, 9761625.
- (52) Liu, D.; Dong, X.; Han, B.; Huang, H.; Qi, M. Cellulose Nanocrystal/Collagen Hydrogels Reinforced by Anisotropic Structure: Shear Viscoelasticity and Related Strengthening Mechanism. *Compos. Commun.* **2020**, *21*, 100374.
- (53) Kumar, A.; Rao, K. M.; Han, S. S. Synthesis of Mechanically Stiff and Bioactive Hybrid Hydrogels for Bone Tissue Engineering Applications. *Chem. Eng. J.* **2017**, *317*, 119–131.
- (54) Zhao, W.; Liu, Y.; Zhang, Z.; Feng, X.; Xu, H.; Xu, J.; Hu, J.; Wang, S.; Wu, Y.; Yan, S. High-Strength, Fast Self-Healing, Aging-Insensitive Elastomers with Shape Memory Effect. *ACS Appl. Mater. Interfaces* **2020**, *12*, 35445–35452.
- (55) Ma, B.; Zhang, H.; Wang, K.; Xu, H.; He, Y.; Wang, X. Influence of ScPLA Microsphere on the Crystallization Behavior of PLLA/PDLA Composites. *Compos. Commun.* **2020**, *21*, 100380.
- (56) Gao, Y.; Shi, L.; Lu, S.; Zhu, T.; Da, X.; Li, Y.; Bu, H.; Gao, G.; Ding, S. Highly Stretchable Organogel Ionic Conductors with Extreme-Temperature Tolerance. *Chem. Mater.* **2019**, *31*, 3257–3264.
- (57) Ding, Y.; Zhang, J.; Chang, L.; Zhang, X.; Liu, H.; Jiang, L. Preparation of High-Performance Ionogels with Excellent Transparency, Good Mechanical Strength, and High Conductivity. *Adv. Mater.* **2017**, *29*, 1704253.
- (58) Zhang, X. F.; Ma, X.; Hou, T.; Guo, K.; Yin, J.; Wang, Z.; Shu, L.; He, M.; Yao, J. Inorganic Salts Induce Thermally Reversible and Anti-Freezing Cellulose Hydrogels. *Angew. Chem., Int. Ed.* **2019**, *58*, 7366–7370.
- (59) Dai, X.; Zhang, Y.; Gao, L.; Bai, T.; Wang, W.; Cui, Y.; Liu, W. A Mechanically Strong, Highly Stable, Thermoplastic, and Self-Healable Supramolecular Polymer Hydrogel. *Adv. Mater.* **2015**, *27*, 3566–3571.
- (60) Liu, Z.; Wan, K.; Zhu, T.; Zhu, J.; Xu, J.; Zhang, C.; Liu, T. Superelastic, Fatigue-Resistant, and Flame-Retardant Spongy Conductor for Human Motion Detection against a Harsh High-

Temperature Condition. *ACS Appl. Mater. Interfaces* **2021**, *13*, 7580–7591.